

Tailored Polyimide–Graphene Nanocomposite as Negative Electrode and Reduced Graphene Oxide as Positive Electrode for Flexible Hybrid Sodium-Ion Capacitors

Qinglan Zhao,[†] Dongfang Yang,[†] Cheng Zhang,[‡] Xuan-He Liu,[§] Xin Fan,[†] Andrew K. Whittaker,[‡] and X. S. Zhao^{*,†}

[†]School of Chemical Engineering, The University of Queensland, Brisbane, QLD 4072, Australia

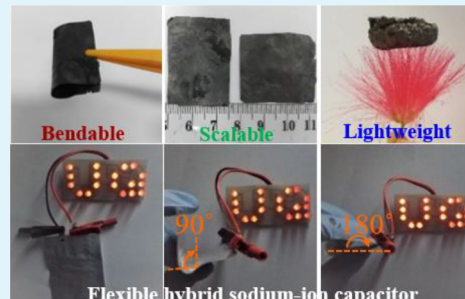
[‡]Australian Institute for Bioengineering and Nanotechnology and ARC Centre of Excellence in Convergent Bio-Nano Science and Technology, The University of Queensland, Brisbane, QLD 4072, Australia

[§]School of Science, China University of Geosciences, Beijing 100083, China

Supporting Information

ABSTRACT: Redox-active polyimide materials hold a great promise for electrochemical energy storage applications, especially for flexible energy storage devices. However, the low utilization efficiency due to poor electrical conductivity of the materials remains one of the greatest challenges. In this work, we designed and prepared polyimide–graphene composite materials and tested their electrochemical properties in sodium-ion capacitors. By manipulating the interfacial chemistry and interactions between the polyimide and graphene, composite electrode materials with different polyimide particle sizes and morphologies were obtained. Sodium-ion storage capacity was significantly improved, from $\sim 50 \text{ mAh g}^{-1}$ for pure polyimide to 225 mAh g^{-1} for a polyimide–graphene composite. A hybrid sodium-ion capacitor fabricated with freestanding polyimide–graphene composite as the negative electrode and reduced graphene oxide as the positive electrode delivered energy densities of 55.5 and 21.5 Wh kg^{-1} at power densities of 395 and 3400 W kg^{-1} , respectively. A flexible sodium-ion capacitor with outstanding mechanical properties was also demonstrated.

KEYWORDS: flexible device, sodium-ion capacitor, polyimide, graphene, composite electrode



INTRODUCTION

Flexible energy storage devices are important components in flexible electronics.^{1,2} It is important to develop cost-effective flexible energy storage devices with both high specific energy and power. Among the various energy storage systems,^{3–5} sodium-ion capacitors (NICs) are of particular importance because they can possess both high specific energy and power and because sodium is a widely available resource. Presently, advanced electrode materials suitable for the NIC technology are being investigated.^{6–14}

Redox polymers are promising sodium-ion storage materials for flexible NICs, due to their flexibility,¹⁵ non-toxicity,¹⁶ low cost,¹⁷ structural adaptability,¹⁸ and lower sensitivity to the large sodium ions.¹⁹ Polyimides (PIs) are cost-effective polymers with functional groups, which have been demonstrated to be electrochemically active for ion storage.^{20,21} However, polyimides have a poor electrical conductivity.²² Thus, a large quantity of conductive carbons (30–60 wt %) is needed in fabrication of polyimide electrodes.^{23,24} This leads to a poor utilization of the electrochemically active sites (functional groups).²⁵ It is thus important to develop polyimide electrodes with significantly improved electrical conductivity.^{20,26} While using nanomaterials, such as nano-

particles, can enhance the accessibility of the electrochemically active sites for redox reactions,^{27,28} these small particles tend to aggregate to form larger ones.

The use of three-dimensional (3D) porous graphene to support nanoparticles is a promising approach to preparing composite electrode materials. Graphene can not only act as a conductive substrate^{29,30} but also provide active sites for nucleation or polymerization.^{31,32} Wei and co-workers²³ demonstrated a facile strategy for fabricating graphene–polyimide composite electrode materials with application potentials as a cathode for flexible lithium batteries. Xu et al.²⁵ reported an in situ polymerization and self-assembly strategy to prepare graphene foam–polyimide composite films as a binder-free cathode for flexible lithium-ion batteries and sodium-ion batteries.

In this paper, we describe a strategy for controlling the morphology and size of polyimide particles by manipulating the interfacial chemistry and interactions between polyimide and graphene. The sodium-ion storage mechanism in the

Received: October 1, 2018

Accepted: November 26, 2018

Published: November 26, 2018



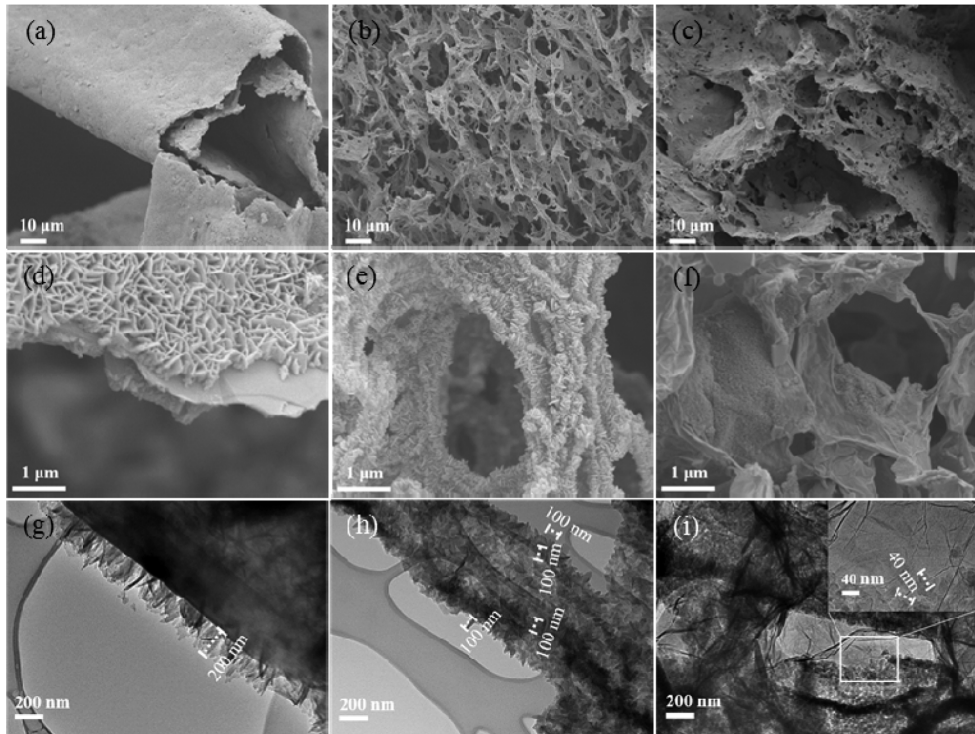
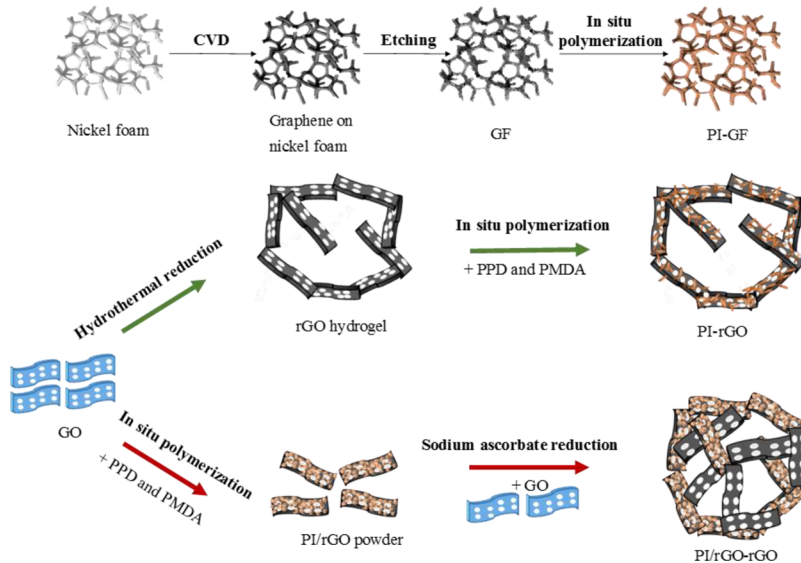
ACS Publications

© 2018 American Chemical Society

43730

DOI: 10.1021/acsami.8b17171

ACS Appl. Mater. Interfaces 2018, 10, 43730–43739

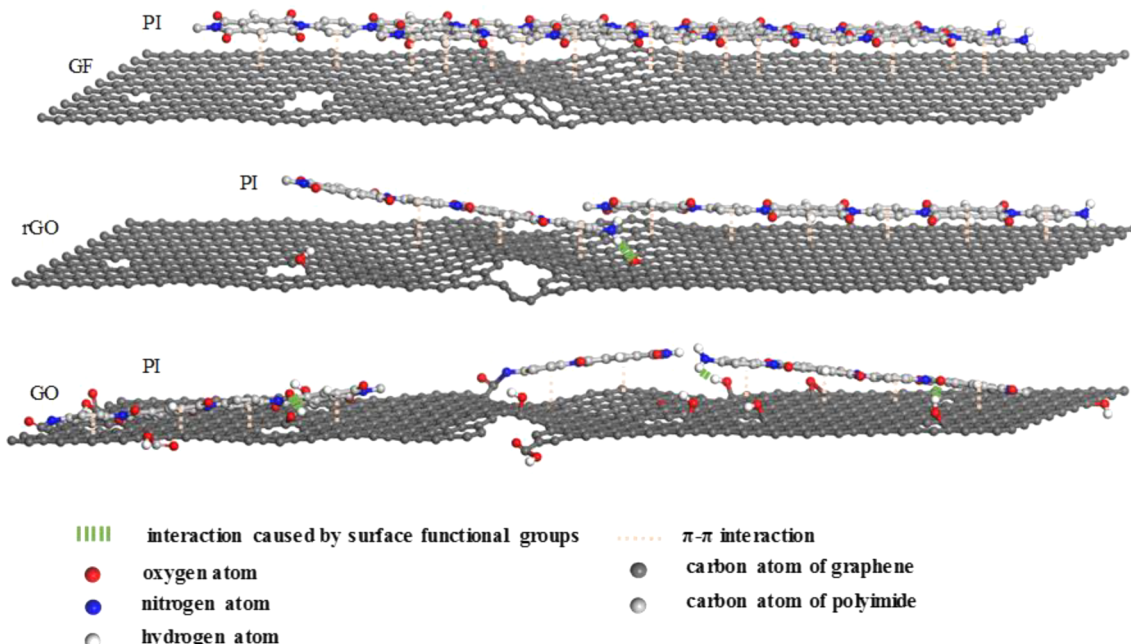
Scheme 1. Schematic Illustration of Preparation of Samples PI-GF, PI-rGO, and PI/rGO-rGO**Figure 1.** (a–f) FESEM images and (g–i) TEM images of (a, d, g) PI-GF, (b, e, h) PI-rGO, and (c, f, i) PI/rGO-rGO at different magnifications (the inset of (i) is an enlarged image of PI/rGO-rGO).

composite was investigated. A sodium-ion capacitor full cell fabricated with the composite as the anode and reduced graphene oxide as the cathode delivered energy densities of 55.5 and 21.5 Wh kg⁻¹ at power densities of 395 and 3400 W kg⁻¹, respectively. A flexible sodium-ion capacitor was also fabricated to demonstrate application potentials for flexible energy storage devices.

RESULTS AND DISCUSSION

Preparation and Characterization of Polyimide–Graphene Nanocomposites. Three freestanding and flexible polyimide–graphene composite samples (Figure S1),

designated as PI-GF (GF, graphene foam), PI-rGO, and PI/rGO-rGO, were prepared in this study. Scheme 1 shows the schematic illustration of the preparation method. The details of the method of preparation can be found in the Supporting Information. The three samples contained a similar content of PI as can be seen from the TGA data shown in Figure S2. The presence of polyimide in the composites was confirmed by the Fourier transform infrared (FTIR) and ¹³C magic angle spinning nuclear magnetic resonance (MAS NMR) spectra depicted in Figure S3. The peak at 1380 cm⁻¹ is due to the stretching vibration of the imide C—N group. The peaks at 1782, 1715, and 723 cm⁻¹ correspond to the asymmetric

Scheme 2. Schematic Illustration of the Mechanism of Formation of the PI-Graphene Composites^a

^aVisual Molecular Dynamics was used to create the graphic.³⁸

stretching vibration (ν_{as}), symmetric stretching vibration (ν_s), and bending vibration (δ) of the imide group C=O, respectively.³³ The peaks in the ^{13}C MAS NMR spectra at 165.0, 137.6, 129.5, and 115.9 ppm are assigned to the imide carbonyl carbon, the non-protonated aromatic carbon of the benzimidazole group, the protonated aromatic benzimidazole carbon, and the N-substituted aromatic carbon, respectively.³⁴

Figure 1 shows the field-emission scanning electron microscopy (FESEM) and transmission electron microscopy (TEM) images of the samples. Flat polyimide nanosheets with an average height of 200 nm grown on both sides of the graphene foam can be clearly seen in Figure 1a, d, and g. The FESEM images of PI-GF shown in Figure S4 confirmed the full and conformal inheritance of continuous topographic features of the nickel foam template. For the sample PI-rGO, the rGO is coated with vertically aligned but smaller protuberant polyimide nanoflakes with an average height of 100 nm (Figure 1b, e, and h). In contrast to the former two nanocomposites, PI/rGO-rGO was made by a two-step method. The 3D framework was constructed with a polyimide/rGO/polyimide sandwich-like structure (Figure S5) embedded in a conductive rGO framework (Figure 1c, f, and i). Polyimide grains with an average diameter of 40 nm were distributed uniformly on the graphene sheets of PI/rGO-rGO. Compared with the pure polyimide particles of $\sim 15\ \mu\text{m}$ in diameter (Figure S6), all the nanocomposites show nanosized polyimide structures in a 3D interconnected porous network. The structure is a result of the surface of graphene providing sufficient nucleation sites for the growth of the polyimide particles,³¹ resulting in a decreased size.³⁵ The uniform distribution of the polyimide was confirmed by the energy-dispersive X-ray (EDX) mapping images (Figure S7).

The structures adopted by the polyimides in PI-GF are profoundly different in size and form from those in PI/rGO-rGO, while the polyimide in PI-rGO has an intermediate shape and size. It is evident that the nature of the interface between the polyimide and the graphene plays an important role in

determining the final structure.^{29,36,37} The surface of the graphene foam (GF) has few functional groups (Figure S8a,b and Table S1), and therefore, interactions at the interface are driven by the $\pi-\pi$ interactions between aromatic rings of the polyimides and GF.²⁹ In the case of GO, the surface contains abundant oxygen- and nitrogen-containing groups (Figure S8a, b,c and Table S1) which are able to interact with the functional groups of the polyimide chains. We conclude that the interactions of functional groups of GO and the polyimide are more specific and stronger than the $\pi-\pi$ interactions. For the rGO with fewer residue surface functional groups (Figure S8a,b and Table S1), $\pi-\pi$ interactions and relatively weaker interactions between functional groups will both play a role.

On the basis of the above observations, a mechanism of formation of the polyimide-graphene nanocomposite materials is proposed and illustrated in Scheme 2. In the formation of PI-GF, the aromatic rings of the polyimide are involved in $\pi-\pi$ interactions with sp^2 hybridized carbons of graphene. The polyimide chains are supposed to continue to grow parallel to the graphene plane at the interface. Then, under the intermolecular force among the polyimides, multiple chains self-assemble to form flat polyimide nanosheets. Finally, with the chains at the interface parallel to the graphene plane, the self-assembled polyimide nanosheets stand perpendicularly on the surface of the GF.

In the case of PI/rGO-rGO, since GO was used in the first step in the synthesis, surface functional groups are believed to be involved. The diamines and dianhydrides undergo in situ polymerization and self-assembly at the interface, under the interaction between the functional groups. At the same time, GO undergoes thermal reduction leading to the removal of surface functional groups, which causes a gradual lessening of interactions between the functional groups and increasing participation of $\pi-\pi$ interactions between the polyimides and GO. The randomly distributed functional groups on the surface of GO lead to random growth and assembly of the

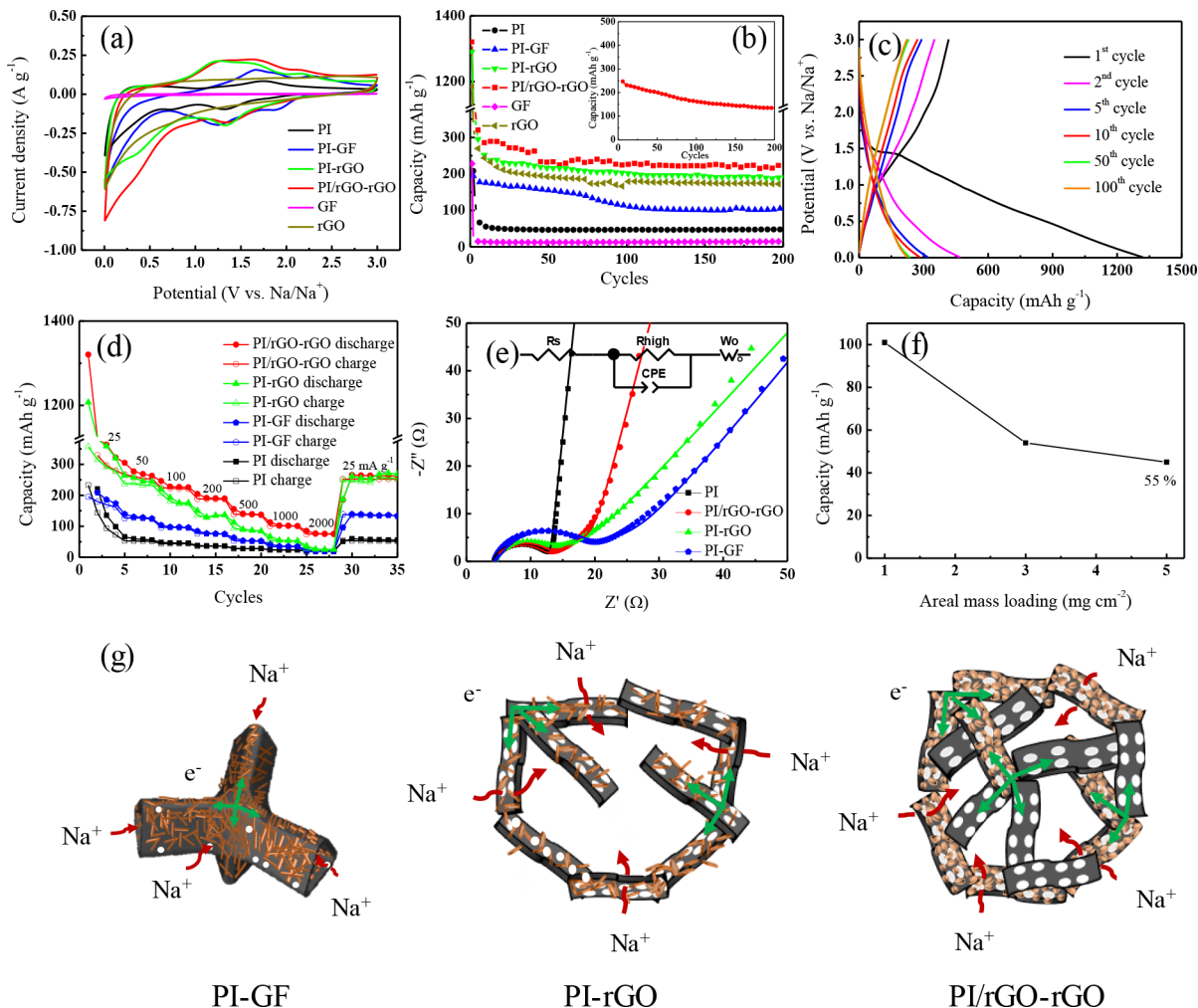


Figure 2. (a) CV curves on the second cycle and (b) cycling performance of PI electrode, PI-GF, PI-rGO, PI/rGO-rGO, GF, and rGO (inset: cycling performance of PI/rGO-rGO at 100 mA g⁻¹ from the 5th cycle); (c) the discharge and charge curves of PI/rGO-rGO at different cycles; (d) the rate performance of the PI electrode, PI-GF, PI-rGO, and PI/rGO-rGO; (e) Nyquist plots for a symmetric cell using two identical electrodes at a state of charge (SOC) of 0% (inset: simulated equivalent circuit); (f) the retention of specific capacity as a function of mass loading for PI/rGO-rGO at 500 mA g⁻¹; and (g) the schematic illustration of pathways for electron conduction (green arrows) and sodium ion diffusion (red arrows) in the 3D polyimide and graphene composites.

polyimides, finally forming irregular-shaped nanograins of PI on the rGO.

The rGO has a content of surface functional groups intermediate between GO and GF (Figure S8a,b and Table S1). In the formation of PI-rGO, the polyimide chains grow parallel to the graphene plane due to extensive $\pi-\pi$ interactions, and the self-assembly of the polyimide chains is affected by interactions between the functional groups of the polyimides and the residue functional groups on the surface of rGO,³² leading to protuberant polyimide nanoflakes standing perpendicularly on the rGO.

Polyimide–Graphene Nanocomposites as the Negative Electrode. The CV profiles between 0.005 and 3.0 V vs Na/Na⁺ of the PI electrode, PI-GF, PI-rGO, and PI/rGO-rGO at a scan rate of 0.2 mV⁻¹ are shown in Figure S9. All first-cycle profiles show a peak at ~1.25 V, which disappeared in the subsequent cycle. This peak is assigned to the formation of a solid electrolyte interface, which may cause the irreversible capacity loss in initial cycles. Except for PI-GF, there is an obvious peak at ~0.25 V, particularly for PI-rGO and PI/rGO-rGO. This peak corresponds to the irreversible trapping of

sodium ions in the carbon black in the PI electrode or surface defects of rGO in PI-rGO and PI/rGO-rGO.^{39,40} Figure 2a displays the CV curves on the second circle of different electrodes plotted for comparison. The GF and rGO electrodes show a quasi-rectangular shape without any peaks. It can be observed that the PI electrode showed the lowest current response while composite PI/rGO-rGO showed the highest current response. The two broad cathodic peaks appearing at potentials of 0.75 and 1.25 V are due to sodiation of the carbonyls to form radical anions and dianions.⁴¹ The broad peak between 1 and 2 V during the reverse anodic scan is due to the desodiation of the sodiated polyimide.

In line with CV results, all the nanocomposites exhibited much higher capacity than the pure polyimide (~50 mAh g⁻¹, Figure 2b). The higher capacity of the composite materials during cycling is due to the decreased size of polyimide particles in the composites, which exposes more active sites for the redox reactions of carbonyl groups with sodium ions.⁴² On the other hand, the higher capacity of PI/rGO-rGO and PI-rGO than PI-GF can be attributed to the contribution from rGO (43 mAh g⁻¹ at the 200th cycle). Sodium ions are stored

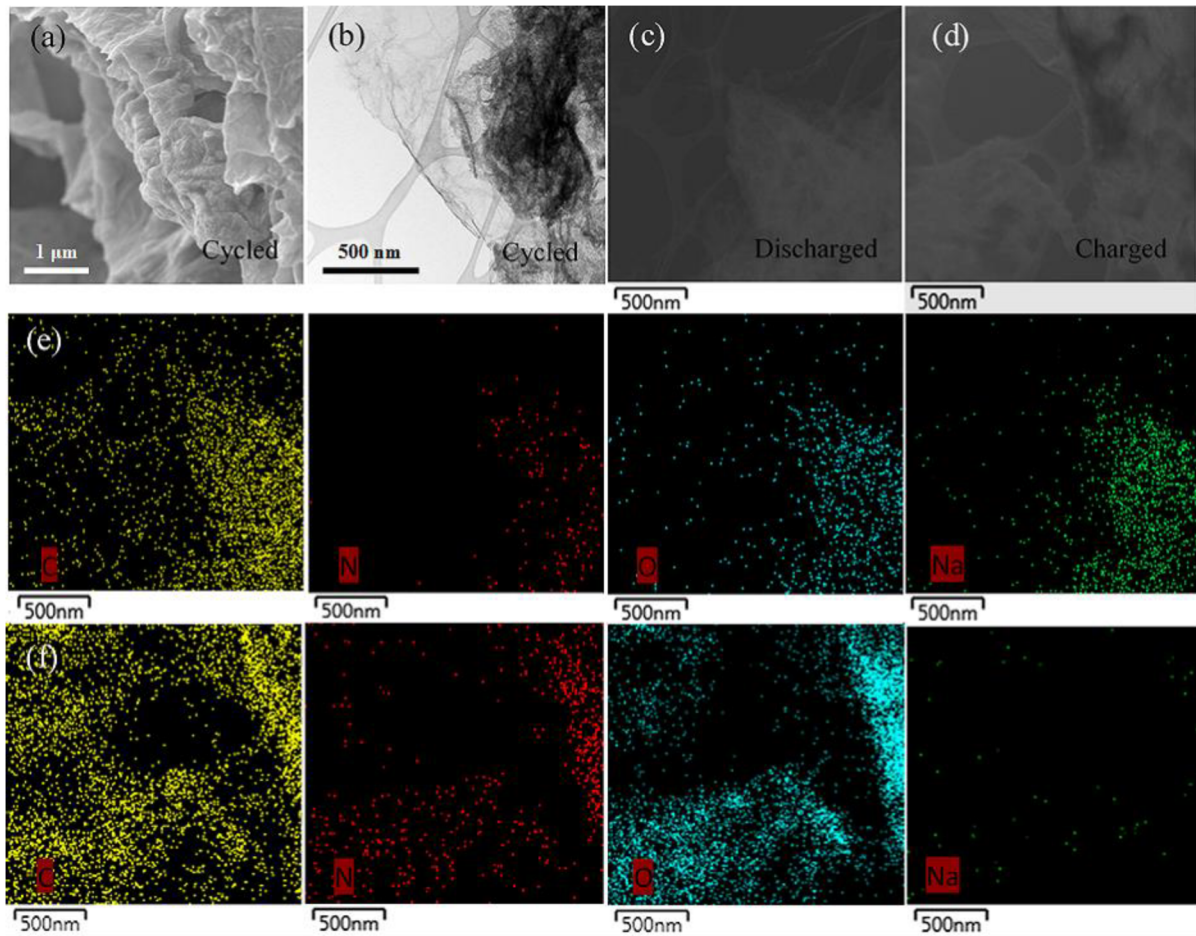


Figure 3. (a) FESEM and (b) TEM images of the PI/rGO-rGO electrode after 200 cycles; the scanning transmission electron microscopy (STEM) images of (c) discharged and (d) charged PI/rGO-rGO electrode; and the EDX mapping images of (e) discharged and (f) charged PI/rGO-rGO electrode.

in the rGO by adsorption on the graphene sheets, interaction with heteroatoms, and intercalation in the interlayers.^{43,44} It should be noted that the current density and specific capacity were only calculated according to the mass of polyimide for PI-GF since GF does not contribute significantly to the charge storage. The narrow interlayer spacing (3.5 Å) and absence of abundant surface functional groups on GF are the main causes of the lower sodium-ion intercalation and adsorption (Figure S10).⁴⁵ However, the calculations for PI-rGO and PI/rGO-rGO were based on the entire composite electrode since rGO contributes significantly to the overall capacity. Among the nanocomposites, the PI/rGO-rGO retained the highest capacity of 225 mAh g⁻¹ at the 200th cycle at 25 mA g⁻¹ and 134 mAh g⁻¹ at the 200th cycle at 100 mA g⁻¹. Additionally, the discharge and charge profiles of PI/rGO-rGO show sloping curves (Figure 2c), indicating fast redox reactions of the PI/rGO-rGO electrode.²² The fast kinetics for the redox reaction during the discharge and charge processes identifies it as a promising electrode for hybrid sodium-ion capacitors.⁴⁶

As expected, all nanocomposites achieved a higher capacity than the pure polyimide at the same current density (Figure 2d). This is not only because of the decreased size of polyimide particles exposing more active sites but also because the 3D interconnected porous framework results in decreased distance diffusion of the electrolyte ions. PI/rGO-rGO shows the best rate performance with a high capacity of 75 mAh g⁻¹ at a high

current density of 2000 mA g⁻¹, demonstrating excellent rate capability of the PI/rGO-rGO electrode.

Electrochemical impedance spectroscopy (EIS) measurements of a symmetric cell with two identical electrodes were conducted to provide impedance data of the electrode–electrolyte interface that is more accurate than that of typical EIS measurements of asymmetric cells with a metal as the counter electrode.⁴⁷ The Nyquist plots in Figure 2e exhibit a depressed semicircle in the high frequency region, a 45° slope in the middle frequency region, and a quasi-vertical line at low frequency, which can be simulated by an equivalent circuit (Figure 2e inset). The intercept on the real axis in the high frequency region is the internal electrolyte resistance (R_s). The 45° slope relates to the Warburg element open circuit terminus (W_o), reflecting the ionic resistance for the electrolyte-filled pores in the electrode.⁴⁸ The depressed semicircle corresponds to the charge-transfer resistance (R_{ct}). A smaller R_{ct} indicates more electron-transfer pathways and faster electrolyte-ion diffusion, which can lead to enhanced cycling stability and rate performance.⁴⁹ The PI/rGO-rGO has nearly the same R_{ct} as the PI electrode using carbon black as the conductive additive, suggesting an excellent inner electrical network built by the rGO in the second preparation step. The more highly developed electron conductive pathways in PI/rGO-rGO account for its superior rate performance compared with the other two composites (Figure 2g). Due to the highly

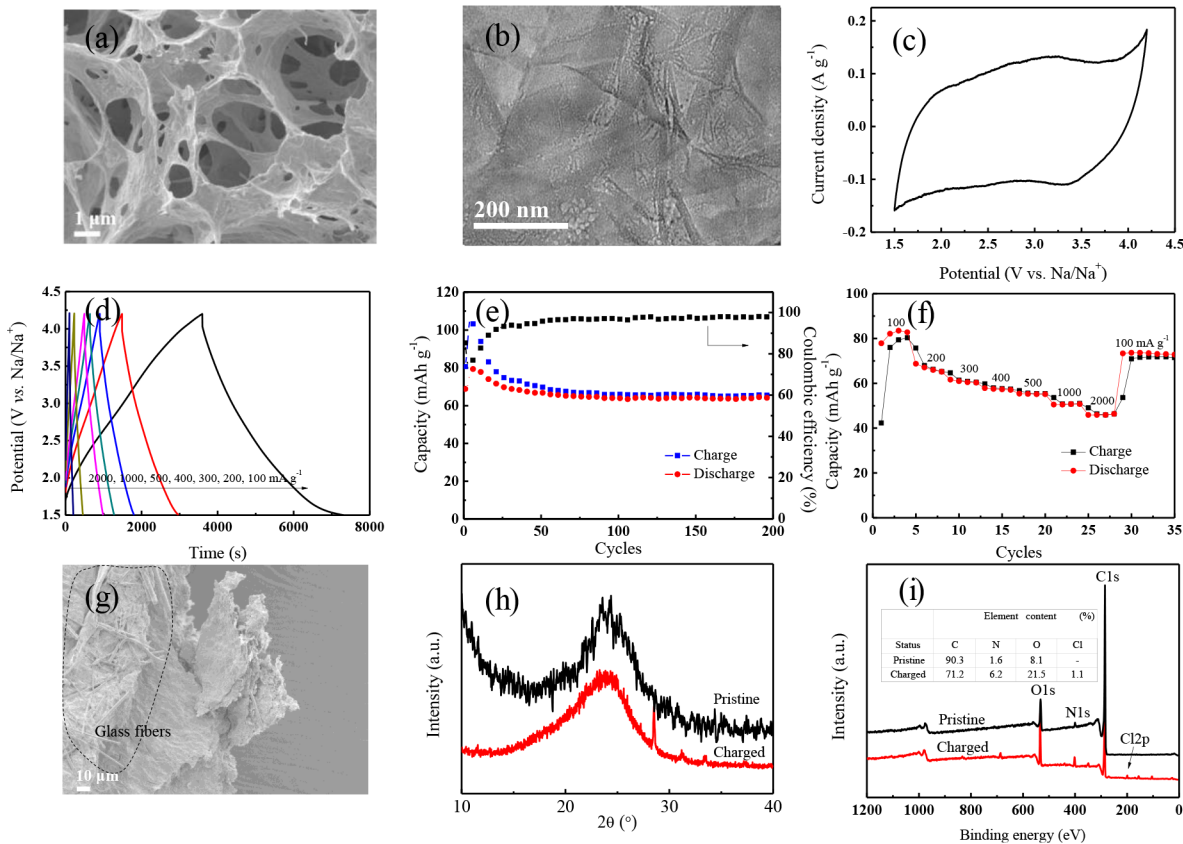


Figure 4. (a) FESEM image, (b) TEM image, (c) CV curve at a scan rate of 1 mV s^{-1} , (d) GCD profiles at different current densities, (e) cycling performance at the current density of 100 mA g^{-1} and (f) rate capability of rGO; (g) the FESEM image of rGO electrode after 200 cycles; and the (h) XRD patterns and (i) X-ray photoelectron spectroscopy (XPS) survey of the pristine rGO electrode and the rGO electrode charged to 4.2 V.

developed 3D interconnected porous and conductive network of PI/rGO-rGO, the capacity retention can remain at 55% when the areal mass loading increased five times from 1 to 5 mg cm^{-2} (Figure 2f), demonstrating great potential for high mass loading in practical applications.

After long-term cycling, the morphology and structure of the PI/rGO-rGO electrode were preserved (Figure 3a–d) compared with the pristine electrode (Figure 1h and i). The EDX mapping images (Figure 3e and f) of the discharged and charged PI/rGO-rGO electrodes confirmed the reversible storage of sodium ions in the composite electrodes.

Reduced Graphene Oxide as the Positive Electrode. Reduced graphene oxide (rGO) displays an interconnected 3D macroporous morphology (Figure 4a) with nanopores on the sheets (Figure 4b), consistent with the results of nitrogen adsorption–desorption measurements (Figure S11). The CV measurements for the rGO positive electrode (Figure 4c) were conducted at a high potential range from 1.5 to 4.2 V (vs Na/Na⁺), which is not favorable for intercalation/deintercalation of the anions.⁵⁰ The current peak at the high potential of 4 V vs Na/Na⁺ may be due to the decomposition of the electrolyte. The CV curve with a very slightly biased rectangular shape and the slightly bent galvanostatic charge and discharge (GCD) profiles (Figure 4d) demonstrated a capacitor-like response. This suggests an electrical double-layer capacitance (EDLC) charge storage mechanism combined with a surface redox reaction.⁵¹ The rGO electrode shows a high capacity of ~70 mAh g^{-1} and nearly 100% Coulombic efficiency at the 200th cycle (Figure 4e). This is significantly higher than the capacity (44 mAh g^{-1}) of a commercial AC (Figure S12). The excellent

rate capability and capacity recovery were also confirmed by the results presented in Figure 4f. A high capacity of 46 mAh g^{-1} was achieved at 2000 mA g^{-1} , and a reversible capacity of 72 mAh g^{-1} was recovered when the current density was reduced to 100 mA g^{-1} . It can be seen from Figure 4g that the morphology of rGO was preserved after long-term cycling. The glass fibers marked in the FESEM image are from the separator. The negligible differences in the X-ray diffraction (XRD) patterns (Figure 4h) between the pristine and charged state confirms lack of intercalation by the perchlorate anions. The sharp peak of the XRD pattern of the charged electrode may come from the impurity. The changes in percentages of chlorine to oxygen are not at the ratio of 1:4 (Figure 4i), which further confirms that the charge storage mechanism is not solely based on EDLC. Therefore, we deduce that the capacity of the rGO electrode operated at high potential range of 1.5–4.2 V arises from the EDLC of perchlorate anions and the pseudocapacitance from reversible surface redox reactions⁵² between the residue surface functional groups and sodium ions.

Electrochemical Performance of a Hybrid Sodium-Ion Capacitor. Following assessment of the performance of the polyimide–graphene nanocomposites in half cells, PI/rGO-rGO was selected as the negative electrode and rGO as the positive electrode to assemble a hybrid capacitor. The mass ratio of positive electrode to negative electrode was set at approximately 3:1, based on the capacities of both electrodes with some overcapacity of the rGO positive electrode to allow better potential stability for the PI/rGO-rGO negative electrode.⁵³ Based on the above study of the negative electrode

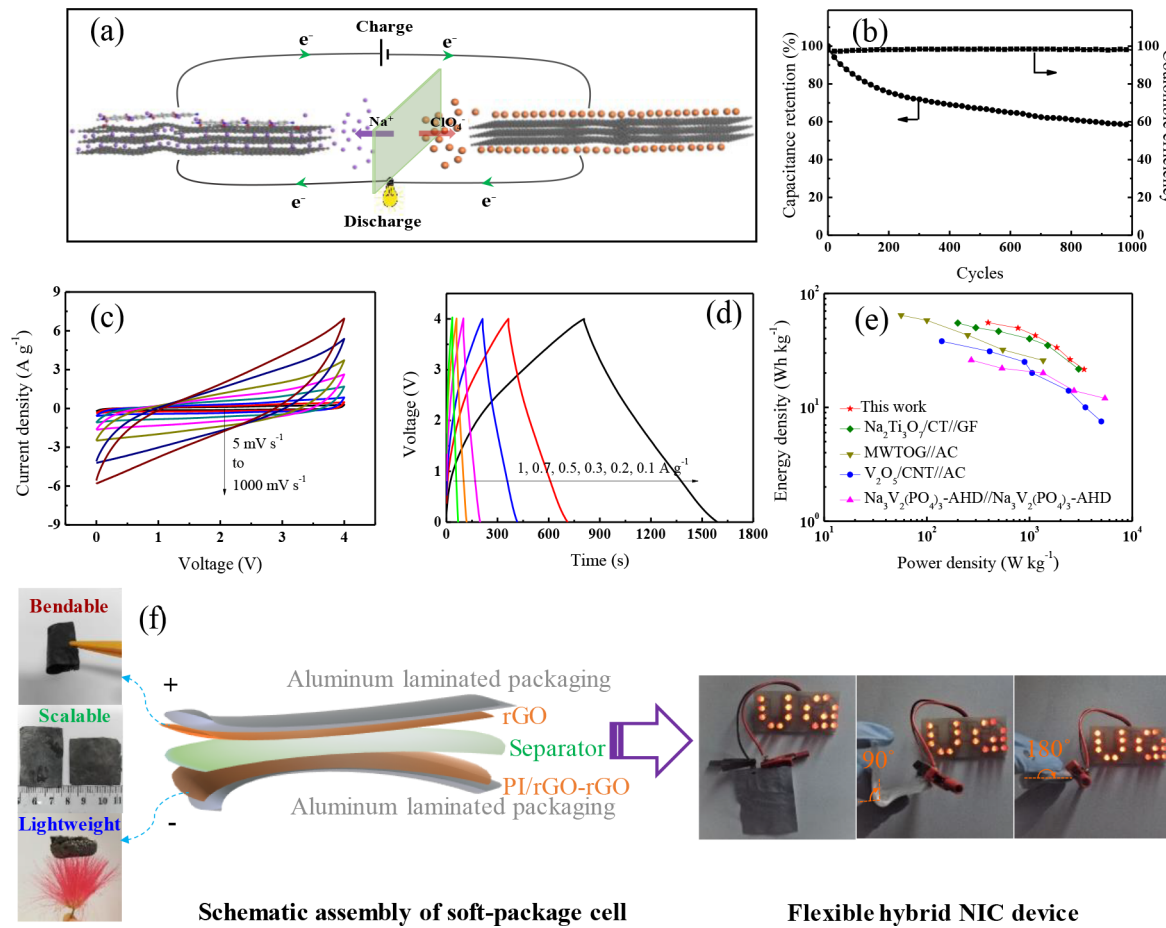


Figure 5. (a) The schematic illustration of the configuration of the PI/rGO-rGO NIC cell (the movement of electrolyte ions showing the discharge process); the electrochemical performance of the PI/rGO-rGO//rGO NIC with (b) cycling performance at current density of 100 mA g^{-1} , (c) CV curves at different scan rates of 5, 10, 20, 50, 100, 200, 500, and 1000 mV s^{-1} , (d) GCD curves at different current densities, (e) gravimetric energy-power density performance in comparison with other reported NICs (MWTOG//AC⁸, $Na_2Ti_3O_7/CT//GF$,⁵⁷ $V_2O_5/CNT//AC$,⁵⁸ and $Na_3V_2(PO_4)_3-AHD//Na_3V_2(PO_4)_3-AHD$,⁵⁹ [MWTOG: TiO₂ meso-cage graphene nanocomposite, CT: carbon textile, GF: reduced graphene oxide film, CNT: carbon nanotube, AHD: ambient hydrolysis deposition]); and (f) the schematic assembly of a soft-package hybrid NIC using flexible freestanding electrodes and its practical application to LED panel. Visual Molecular Dynamics was used to create the graphic in (a).³⁸

and positive electrode, a working mechanism of the PI/rGO-rGO NIC is proposed (Figure 5a). Upon charging, the PI/rGO-rGO negative electrode experiences a reversible redox reaction of sodium ions via enolization with the carbonyl groups of the polyimide and reversible storage of sodium ions in rGO, while the rGO positive electrode adsorbs perchlorate anions reversibly and releases sodium ions from the functional groups on the surface. During the subsequent discharge, the reverse process occurs.

It should be noted that analyses of the electrochemical tests of the hybrid capacitor were based on the overall mass or the total volume of the freestanding PI/rGO-rGO negative electrode and rGO positive electrode. The hybrid NIC shows a capacitance retention of $\sim 60\%$ at the 1000th cycle at a wide voltage of 4 V, with a high Coulombic efficiency near to 100% (Figure 5b). Such a wide voltage can cause a capacity decay, which may result from the degradation of the residue oxygen functionalities on the surface of rGO.^{54,55} The decomposition of electrolyte might be also responsible for the capacity decay, since the current peak of rGO electrode was observed at the high potential which may be due to the electrolyte decomposition. The CV curves (Figure 5c) generally display a rectangular shape, indicating that the

hybrid NIC mainly shows capacitive behavior. The shape of the CV curves is retained at a high scan rate of 1000 mV s^{-1} , demonstrating high power capability of the hybrid NIC.⁵⁶ Figure 5d shows negligible initial voltage loss (IR drop) of the discharge profiles, suggesting a low internal resistance and fast current–voltage response of the hybrid NIC. A high gravimetric energy density of 55.5 Wh kg^{-1} was achieved at a gravimetric power density of 395 W kg^{-1} , and the hybrid NIC can retain a gravimetric energy density of 21.5 Wh kg^{-1} at the gravimetric power density of 3400 W kg^{-1} (Figure 5e). Such a combination of high gravimetric energy and power densities is superior to many other NICs (Figure 5e). The volumetric performance of the NIC was also evaluated, as is shown in Figure S13. High volumetric energy densities of 58.8 and 20.7 Wh L^{-1} were achieved at the gravimetric power densities of 426 and 3546 W L^{-1} , respectively. The electrochemical performance demonstrated that this hybrid system that integrates a battery-like component and capacitor-like component is promising to overcome the challenges of the capacitance mismatch and sluggish kinetics, bridging the gap between batteries and capacitors.

To test the potential of the hybrid NIC in practical applications, larger-sized electrodes were made by increasing

10 times the amounts of reagents in assembling soft-package hybrid NIC cells (Figure 5f). The scalable freestanding electrode was very flexible and very light, for example, freestanding on a Persian silk flower. The flexible hybrid NIC can light up an electronic device containing 18 light-emitting diode (LED) lamps under different bending statuses after 1 min charge. The NIC shows no obvious change for the charge and discharge curves at the bending angles ranging from 0° to 180° (Figure S14a). As is shown in Figure S14b, the NIC kept a capacitance retention of 57% when the mass loading was increased from 6.2 to 13.1 mg cm⁻². The capacitance of the NIC shows negligible changes within the temperature range from 25 to 55 °C. The NIC demonstrates good production scalability of the electrode materials and great potential for application in flexible electronic devices.

CONCLUSIONS

In summary, polyimide–graphene nanocomposites with different polyimide particle sizes (ranging from ca. 40 to 200 nm) were prepared using different graphene substrates. A flexible, freestanding, and light polyimide–graphene nanocomposite prepared using the two-step self-assembly method exhibited a capacity of 225 mAh g⁻¹ at the 200th cycle in sodium-ion batteries, much higher than that of the pure polyimide (~50 mAh g⁻¹). This remarkable improvement in sodium ion storage capacity is due to the small particle size of the polyimide grown in the graphene framework and the high conductivity of the graphene. This preparation method can be scalable for mass production of high-performance freestanding polyimide–graphene nanocomposite electrodes, making commercialization feasible. It should also be noted that the entire synthesis process is very simple and green without introduction of any chemicals harmful to the environment. In addition, the reduced graphene oxide can be a suitable positive electrode, presenting a much higher capacity (~70 mAh g⁻¹) than commercial activated carbons (44 mAh g⁻¹) via electrical double layer capacitive and pseudocapacitive mechanisms. A flexible hybrid sodium-ion capacitor was assembled using the freestanding polyimide–graphene nanocomposite as the negative electrode and reduced graphene oxide as the positive electrode. A high energy density of 55.5 Wh kg⁻¹ at a power density of 395 W kg⁻¹ and energy density of 21.5 Wh kg⁻¹ at a power density of 3400 W kg⁻¹ were achieved, outperforming many other sodium-ion capacitors. This paper demonstrates an innovative and scalable strategy for synthesizing polyimide–graphene composite electrode materials for next-generation, green, and flexible energy storage devices.

ASSOCIATED CONTENT

Supporting Information

The Supporting Information is available free of charge on the ACS Publications website at DOI: [10.1021/acsami.8b17171](https://doi.org/10.1021/acsami.8b17171).

Experimental section and additional figures and table, involving sample characterizations and electrochemical measurements ([PDF](#))

AUTHOR INFORMATION

Corresponding Author

*E-mail: george.zhao@uq.edu.au.

ORCID

Qinglan Zhao: [0000-0003-0464-3655](https://orcid.org/0000-0003-0464-3655)

Cheng Zhang: [0000-0002-2722-7497](https://orcid.org/0000-0002-2722-7497)

Andrew K. Whittaker: [0000-0002-1948-8355](https://orcid.org/0000-0002-1948-8355)

X. S. Zhao: [0000-0002-1276-5858](https://orcid.org/0000-0002-1276-5858)

Notes

The authors declare no competing financial interest.

ACKNOWLEDGMENTS

This research was supported by project ARC-FL170100101. Q.Z. also gives thanks for the Research Training Program Scholarship and UQ Graduate School Scholarship. The Australian Microscopy and Microanalysis Research Facility at the UQ Centre for Microscopy and Microanalysis are gratefully acknowledged for their facilities and scientific and technical assistance. The Australian National Fabrication Facility, Queensland Node, is acknowledged for providing access to equipment. Visual Molecular Dynamics was developed by the Theoretical and Computational Biophysics Group in the Beckman Institute for Advanced Science and Technology at the University of Illinois at Urbana-Champaign.

REFERENCES

- (1) Yi, F.; Ren, H.; Shan, J.; Sun, X.; Wei, D.; Liu, Z. Wearable Energy Sources Based on 2D Materials. *Chem. Soc. Rev.* **2018**, *47*, 3152–3188.
- (2) Li, W.; Xu, X.; Liu, C.; Tekell, M. C.; Ning, J.; Guo, J.; Zhang, J.; Fan, D. Ultralight and Binder-Free All-Solid-State Flexible Supercapacitors for Powering Wearable Strain Sensors. *Adv. Funct. Mater.* **2017**, *27*, 1702738.
- (3) Dong, S.; Li, H.; Wang, J.; Zhang, X.; Ji, X. Improved Flexible Li-Ion Hybrid Capacitors: Techniques for Superior Stability. *Nano Res.* **2017**, *10*, 4448–4456.
- (4) Xia, Q.; Yang, H.; Wang, M.; Yang, M.; Guo, Q.; Wan, L.; Xia, H.; Yu, Y. High Energy and High Power Lithium-Ion Capacitors Based on Boron and Nitrogen Dual-Doped 3D Carbon Nanofibers as Both Cathode and Anode. *Adv. Energy Mater.* **2017**, *7*, 1701336.
- (5) Chen, Q.; Sun, S.; Zhai, T.; Yang, M.; Zhao, X.; Xia, H. Yolk-Shell NiS₂ Nanoparticle-Embedded Carbon Fibers for Flexible Fiber-Shaped Sodium Battery. *Adv. Energy Mater.* **2018**, *8*, 1800054.
- (6) Yang, Q.; Cui, S.; Ge, Y.; Tang, Z.; Liu, Z.; Li, H.; Li, N.; Zhang, H.; Liang, J.; Zhi, C. Porous Single-Crystal NaTi₂(PO₄)₃ via Liquid Transformation of TiO₂ Nanosheets for Flexible Aqueous Na-ion Capacitor. *Nano Energy* **2018**, *50*, 623–631.
- (7) Xu, D.; Chao, D.; Wang, H.; Gong, Y.; Wang, R.; He, B.; Hu, X.; Fan, H. J. Flexible Quasi-Solid-State Sodium-Ion Capacitors Developed Using 2D Metal-Organic-Framework Array as Reactor. *Adv. Energy Mater.* **2018**, *8*, 1702769.
- (8) Le, Z.; Liu, F.; Nie, P.; Li, X.; Liu, X.; Bian, Z.; Chen, G.; Wu, H. B.; Lu, Y. Pseudocapacitive Sodium Storage in Mesoporous Single-Crystal-like TiO₂-Graphene Nanocomposite Enables High-Performance Sodium-Ion Capacitors. *ACS Nano* **2017**, *11*, 2952–2960.
- (9) Long, Y.; Yang, J.; Gao, X.; Xu, X.; Fan, W.; Yang, J.; Hou, S.; Qian, Y. Solid-Solution Anion-Enhanced Electrochemical Performances of Metal Sulfides/Selenides for Sodium-Ion Capacitors: The Case of FeS_{2-x}Se_x. *ACS Appl. Mater. Interfaces* **2018**, *10*, 10945–10954.
- (10) Yin, J.; Qi, L.; Wang, H. Sodium Titanate Nanotubes as Negative Electrode Materials for Sodium-Ion Capacitors. *ACS Appl. Mater. Interfaces* **2012**, *4*, 2762–2768.
- (11) Wang, Q.; Wen, Z. H.; Li, J. H. A Hybrid Supercapacitor Fabricated with a Carbon Nanotube Cathode and a TiO₂-B Nanowire Anode. *Adv. Funct. Mater.* **2006**, *16*, 2141–2146.
- (12) Wang, H.; Zhu, C.; Chao, D.; Yan, Q.; Fan, H. Nonaqueous Hybrid Lithium-Ion and Sodium-Ion Capacitors. *Adv. Mater.* **2017**, *29*, 1702093.
- (13) Li, Y.; Wang, H.; Huang, B.; Wang, L.; Wang, R.; He, B.; Gong, Y.; Hu, X. Mo₂C-Induced Solid-Phase Synthesis of Ultrathin MoS₂

- Nanosheet Arrays on Bagasse-Derived Porous Carbon Frameworks for High-Energy Hybrid Sodium-Ion Capacitors. *J. Mater. Chem. A* **2018**, *6*, 14742–14751.
- (14) Liang, T.; Wang, H.; Xu, D.; Liao, K.; Wang, R.; He, B.; Gong, Y.; Yan, C. High-Energy Flexible Quasi-Solid-State Lithium-Ion Capacitors Enabled by a Freestanding rGO-Encapsulated Fe_3O_4 Nanocube Anode and a Holey rGO Film Cathode. *Nanoscale* **2018**, *10*, 17814–17823.
- (15) Nyholm, L.; Nyström, G.; Mihryanyan, A.; Strømme, M. Toward Flexible Polymer and Paper-Based Energy Storage Devices. *Adv. Mater.* **2011**, *23*, 3751–3769.
- (16) Lee, B.; Kang, K. Materials Science: Long-Lived Electrodes for Plastic Batteries. *Nature* **2017**, *549*, 339–340.
- (17) Snook, G. A.; Kao, P.; Best, A. S. Conducting-Polymer-Based Supercapacitor Devices and Electrodes. *J. Power Sources* **2011**, *196*, 1–12.
- (18) Matsumoto, A.; Nagahama, S.; Odani, T. Molecular Design and Polymer Structure Control Based on Polymer Crystal Engineering. Topochemical Polymerization of 1,3-Diene Mono- and Dicarboxylic Acid Derivatives Bearing a Naphthylmethylammonium Group as the Counterion. *J. Am. Chem. Soc.* **2000**, *122*, 9109–9119.
- (19) Song, Z.; Zhou, H. Towards Sustainable and Versatile Energy Storage Devices: an Overview of Organic Electrode Materials. *Energy Environ. Sci.* **2013**, *6*, 2280–2301.
- (20) Wu, H.; Meng, Q.; Yang, Q.; Zhang, M.; Lu, K.; Wei, Z. Large-Area Polyimide/SWCNT Nanocable Cathode for Flexible Lithium-Ion Batteries. *Adv. Mater.* **2015**, *27*, 6504–6510.
- (21) Song, Z.; Zhan, H.; Zhou, Y. Polyimides: Promising Energy-Storage Materials. *Angew. Chem.* **2010**, *122*, 8622–8626.
- (22) Wang, H.; Yuan, S.; Ma, D.; Huang, X.; Meng, F.; Zhang, X. Tailored Aromatic Carbonyl Derivative Polyimides for High-Power and Long-Cycle Sodium-Organic Batteries. *Adv. Energy Mater.* **2014**, *4*, 1301651.
- (23) Meng, Y.; Wu, H.; Zhang, Y.; Wei, Z. A Flexible Electrode Based on a Three-Dimensional Graphene Network-Supported Polyimide for Lithium-Ion Batteries. *J. Mater. Chem. A* **2014**, *2*, 10842–10846.
- (24) Peng, C.; Ning, G. H.; Su, J.; Zhong, G.; Tang, W.; Tian, B.; Su, C.; Yu, D.; Zu, L.; Yang, J.; Ng, M. F.; Hu, Y. S.; Yang, Y.; Armand, M.; Loh, K. P. Reversible Multi-Electron Redox Chemistry of π -Conjugated N-Containing Heteroaromatic Molecule-Based Organic Cathodes. *Nat. Energy* **2017**, *2*, 17074.
- (25) Huang, Y.; Li, K.; Liu, J.; Zhong, X.; Duan, X.; Shakir, I.; Xu, Y. Three-Dimensional Graphene/Polyimide Composite-Derived Flexible High-Performance Organic Cathode for Rechargeable Lithium and Sodium Batteries. *J. Mater. Chem. A* **2017**, *5*, 2710–2716.
- (26) Yu, P.; Zhao, X.; Huang, Z.; Li, Y.; Zhang, Q. Free-Standing Three-Dimensional Graphene and Polyaniline Nanowire Arrays Hybrid Foams for High-Performance Flexible and Lightweight Supercapacitors. *J. Mater. Chem. A* **2014**, *2*, 14413–14420.
- (27) Xu, Y.; Zhou, M.; Lei, Y. Organic Materials for Rechargeable Sodium-Ion Batteries. *Mater. Today* **2018**, *21*, 60–78.
- (28) Li, T.; Li, L.; Cao, Y. L.; Ai, X. P.; Yang, H. X. Reversible Three-Electron Redox Behaviors of FeF_3 Nanocrystals as High-Capacity Cathode-Active Materials for Li-Ion Batteries. *J. Phys. Chem. C* **2010**, *114*, 3190–3195.
- (29) Nardecchia, S.; Carriazo, D.; Ferrer, M. L.; Gutiérrez, M. C.; del Monte, F. Three Dimensional Macroporous Architectures and Aerogels Built of Carbon Nanotubes and/or Graphene: Synthesis and Applications. *Chem. Soc. Rev.* **2013**, *42*, 794–830.
- (30) Zhu, Z.; Chen, J. Review—Advanced Carbon-Supported Organic Electrode Materials for Lithium (Sodium)-Ion Batteries. *J. Electrochem. Soc.* **2015**, *162*, A2393–A2405.
- (31) Zhao, G.; Li, X.; Huang, M.; Zhen, Z.; Zhong, Y.; Chen, Q.; Zhao, X.; He, Y.; Hu, R.; Yang, T.; Zhang, R.; Li, C.; Kong, J.; Xu, J. B.; Ruoff, R. S.; Zhu, H. The Physics and Chemistry of Graphene-on-Surfaces. *Chem. Soc. Rev.* **2017**, *46*, 4417–4449.
- (32) Wang, M.; Duan, X.; Xu, Y.; Duan, X. Functional Three-Dimensional Graphene/Polymer Composites. *ACS Nano* **2016**, *10*, 7231–7247.
- (33) Baumgartner, B.; Bojdys, M. J.; Unterlass, M. M. Geomimetics for Green Polymer Synthesis: Highly Ordered Polyimides via Hydrothermal Techniques. *Polym. Chem.* **2014**, *5*, 3771–3776.
- (34) Brock, T.; Sherrington, D. C.; Swindell, J. Synthesis and Characterisation of Porous Particulate Polyimides. *J. Mater. Chem.* **1994**, *4*, 229–236.
- (35) McGuire, K. S.; Lim, G. B.; Lloyd, D. R. Microporous Membrane Formation via Thermally-Induced Phase Separation. VII. Effect of Dilution, Cooling Rate, and Nucleating Agent Addition on Morphology. *J. Membr. Sci.* **1993**, *79*, 27–34.
- (36) Sun, J.; Klechikov, A.; Moise, C.; Prodana, M.; Enachescu, M.; Talyzin, A. V. A Molecular Pillar Approach to Grow Vertical Covalent Organic Framework Nanosheets on Graphene: Hybrid Materials for Energy Storage. *Angew. Chem.* **2018**, *130*, 1046–1050.
- (37) Wu, J.; Zhang, Q.; Wang, J.; Huang, X.; Bai, H. A Self-Assembly Route to Porous Polyaniline/Reduced Graphene Oxide Composite Materials with Molecular-Level Uniformity for High-Performance Supercapacitors. *Energy Environ. Sci.* **2018**, *11*, 1280–1286.
- (38) Humphrey, W.; Dalke, A.; Schulten, K. VMD: Visual Molecular Dynamics. *J. Mol. Graphics* **1996**, *14*, 33–38.
- (39) Luo, X. F.; Yang, C. H.; Peng, Y. Y.; Pu, N. W.; Ger, M. D.; Hsieh, C. T.; Chang, J. K. Graphene Nanosheets, Carbon Nanotubes, Graphite, and Activated Carbon as Anode Materials for Sodium-Ion Batteries. *J. Mater. Chem. A* **2015**, *3*, 10320–10326.
- (40) Jian, Z.; Bommier, C.; Luo, L.; Li, Z.; Wang, W.; Wang, C.; Greaney, P. A.; Ji, X. Insights on the Mechanism of Na-Ion Storage in Soft Carbon Anode. *Chem. Mater.* **2017**, *29*, 2314–2320.
- (41) Zhao, Q.; Gaddam, R. R.; Yang, D.; Strounina, E.; Whittaker, A. K.; Zhao, X. S. Pyromellitic Dianhydride-Based Polyimide Anodes for Sodium-Ion Batteries. *Electrochim. Acta* **2018**, *265*, 702–708.
- (42) Luo, C.; Zhu, Y.; Xu, Y.; Liu, Y.; Gao, T.; Wang, J.; Wang, C. Graphene Oxide Wrapped Croconic Acid Disodium Salt for Sodium Ion Battery Electrodes. *J. Power Sources* **2014**, *250*, 372–378.
- (43) Wang, Y. X.; Chou, S. L.; Liu, H. K.; Dou, S. X. Reduced Graphene Oxide with Superior Cycling Stability and Rate Capability for Sodium Storage. *Carbon* **2013**, *57*, 202–208.
- (44) Chen, T.; Ma, Y.; Guo, Q.; Yang, M.; Xia, H. A Facile Sol-Gel Route to Prepare Functional Graphene Nanosheets Anchored with Homogeneous Cobalt Sulfide Nanoparticles as Superb Sodium-Ion Anodes. *J. Mater. Chem. A* **2017**, *5*, 3179–3185.
- (45) Wen, Y.; He, K.; Zhu, Y.; Han, F.; Xu, Y.; Matsuda, I.; Ishii, Y.; Cumings, J.; Wang, C. Expanded Graphite as Superior Anode for Sodium-Ion Batteries. *Nat. Commun.* **2014**, *5*, 4033.
- (46) Wang, Y. X.; Chou, S. L.; Wexler, D.; Liu, H. K.; Dou, S. X. High-Performance Sodium-Ion Batteries and Sodium-Ion Pseudocapacitors Based on MoS_2 /Graphene Composites. *Chem. - Eur. J.* **2014**, *20*, 9607–9612.
- (47) Ogiara, N.; Kawauchi, S.; Okuda, C.; Itou, Y.; Takeuchi, Y.; Ukyo, Y. Theoretical and Experimental Analysis of Porous Electrodes for Lithium-Ion Batteries by Electrochemical Impedance Spectroscopy Using a Symmetric Cell. *J. Electrochem. Soc.* **2012**, *159*, A1034–A1039.
- (48) Sun, H.; Mei, L.; Liang, J.; Zhao, Z.; Lee, C.; Fei, H.; Ding, M.; Lau, J.; Li, M.; Wang, C.; Xu, X.; Hao, G.; Papandrea, B.; Shakir, I.; Dunn, B.; Huang, Y.; Duan, X. Three-Dimensional Holey-Graphene/Niobia Composite Architectures for Ultrahigh-Rate Energy Storage. *Science* **2017**, *356*, 599–604.
- (49) Jiao, X.; Hao, Q.; Xia, X.; Lei, W.; Ouyang, Y.; Ye, H.; Mandler, D. Free-Standing Hybrid Graphene Paper Encapsulating Nanostructures for High Cycle-Life Supercapacitors. *ChemSusChem* **2018**, *11*, 907–915.
- (50) Shao, Y.; Xiao, J.; Wang, W.; Engelhard, M.; Chen, X.; Nie, Z.; Gu, M.; Saraf, L. V.; Exarhos, G.; Zhang, J. G.; Liu, J. Surface-Driven Sodium Ion Energy Storage in Nanocellular Carbon Foams. *Nano Lett.* **2013**, *13*, 3909–3914.

- (51) Gogotsi, Y.; Penner, R. M. Energy Storage in Nanomaterials—Capacitive, Pseudocapacitive, or Battery-like? *ACS Nano* **2018**, *12*, 2081–2083.
- (52) Wang, H.; Mitlin, D.; Ding, J.; Li, Z.; Cui, K. Excellent Energy-Power Characteristics from a Hybrid Sodium Ion Capacitor Based on Identical Carbon Nanosheets in Both Electrodes. *J. Mater. Chem. A* **2016**, *4*, 5149–5158.
- (53) Dall'Agnese, Y.; Taberna, P. L.; Gogotsi, Y.; Simon, P. Two-Dimensional Vanadium Carbide (MXene) as Positive Electrode for Sodium-Ion Capacitors. *J. Phys. Chem. Lett.* **2015**, *6*, 2305–2309.
- (54) Zhao, Q.; Yang, D.; Whittaker, A. K.; Zhao, X. S. A Hybrid Sodium-Ion Capacitor with Polyimide as Anode and Polyimide-Derived Carbon as Cathode. *J. Power Sources* **2018**, *396*, 12–18.
- (55) Ding, J.; Wang, H.; Li, Z.; Cui, K.; Karpuzov, D.; Tan, X.; Kohandehghan, A.; Mitlin, D. Peanut Shell Hybrid Sodium Ion Capacitor with Extreme Energy-Power Rivals Lithium Ion Capacitors. *Energy Environ. Sci.* **2015**, *8*, 941–955.
- (56) Salunkhe, R. R.; Tang, J.; Kamachi, Y.; Nakato, T.; Kim, J. H.; Yamauchi, Y. Asymmetric Supercapacitors Using 3D Nanoporous Carbon and Cobalt Oxide Electrodes Synthesized from a Single Metal-Organic Framework. *ACS Nano* **2015**, *9*, 6288–6296.
- (57) Dong, S.; Shen, L.; Li, H.; Pang, G.; Dou, H.; Zhang, X. Flexible Sodium-Ion Pseudocapacitors Based on 3D $\text{Na}_2\text{Ti}_3\text{O}_7$ Nanosheet Arrays/Carbon Textiles Anodes. *Adv. Funct. Mater.* **2016**, *26*, 3703–3710.
- (58) Chen, Z.; Augustyn, V.; Jia, X.; Xiao, Q.; Dunn, B.; Lu, Y. High-Performance Sodium-Ion Pseudocapacitors Based on Hierarchically Porous Nanowire Composites. *ACS Nano* **2012**, *6*, 4319–4327.
- (59) Jian, Z.; Raju, V.; Li, Z.; Xing, Z.; Hu, Y. S.; Ji, X. A High-Power Symmetric Na-Ion Pseudocapacitor. *Adv. Funct. Mater.* **2015**, *25*, 5778–5785.